General Disclaimer

One or more of the Following Statements may affect this Document

- This document has been reproduced from the best copy furnished by the organizational source. It is being released in the interest of making available as much information as possible.

- This document may contain data, which exceeds the sheet parameters. It was furnished in this condition by the organizational source and is the best copy available.

- This document may contain tone-on-tone or color graphs, charts and/or pictures, which have been reproduced in black and white.

- This document is paginated as submitted by the original source.

- Portions of this document are not fully legible due to the historical nature of some of the material. However, it is the best reproduction available from the original submission.

Bending-Torsion Flutter of a Highly Swept Advanced Turboprop

O. Mehmed, K. R. V. Kaza, J. F. Lubomski, and R. E. Kielb
Lewis Research Center
Cleveland, Ohio

NASA

BENDING-TORSION FLUTTER OF A HIGHLY
SWEPT ADVANCED TURBOPROP

By

O. Mehmed, K. R. V. Kaza,
J. F. Lubomski, and R.E. Kielb

National Aeronautics and Space Administration
Lewis Research Center
Cleveland, Ohio 44135

ABSTRACT

Experimental and analytical results are presented for a bending-torsion flutter phenomena encountered during wind-tunnel testing of a ten-bladed, advanced, high-speed propeller (turboprop) model with thin airfoil sections, high blade sweep, low aspect ratio, high solidity and transonic tip speeds. Flutter occured at free-stream Mach numbers of 0.6 and greater and when the relative tip Mach number (based on vector sum of axial and tangential velocities) reached a value of about one. The experiment also included two and five-blade configurations. The data indicate that aerodynamic cascade effects have a strong destabilizing influence on the flutter boundary. The data was correlated with analytical results which include aerodynamic cascade effects and good agreement was found.

INTRODUCTION

In the past, the main concerns with respect to the aeroelastic stability of conventional metal propeller blades have been stall flutter and wake flutter. Classical flutter, which generally involves a coupling between bending and torsion motions, has not been a major concern because the classical flutter boundary has been well outside the conventional propeller operating range. However, this may not be true for advanced propellers which have different characteristics and operate at high subsonic Mach numbers. Recent wind tunnel test results of an advanced turboprop model (called SR-5) with highly swept, flexible blades have demonstrated classical flutter in the propeller operating range.

Most experimental studies that relate to propeller blade flutter were accomplished in the years from 1945 to 1956. These studies ended when the propeller was replaced by the turbojet as the predominant means of commercial and military aircraft propulsion. Some of the significant experimental results from this period are given in (1 to 4)*. Because of the potential for very high propulsive efficiency at cruise speeds up to Mach 0.8, advanced forms of the propeller are again being seriously considered for aircraft propulsion (5). This renewed interest has been sparked by rising fuel costs. In order to obtain maximum aerodynamic and acoustic performance, the trend in advanced high speed propeller design has been toward thin, swept blades of complicated structural design. To establish the technology required for the

---

*Numbers in parentheses designate references at end of paper.

successful design of advanced propellers, a research program is in progress at NASA Lewis Research Center that includes both experimental and analytical aeroelastic studies.

As part of this research program, aeroelastic stability experiments have been completed at the Lewis 8- by 6-Foot Wind Tunnel from Mach 0.36 to 0.85 with advanced turboprop models. Three models designed for aerodynamic and acoustic experiments of about 1/7 full-size were used. These models were not aeroelastically scaled. However, the experimental aeroelastic stability data has been useful in understanding the blade characteristics that most influence the flutter margin, and in developing analyses for predicting the high speed flutter of advanced turboprop type blades.

The most highly swept model, SR-5, exhibited a bending-torsion flutter phenomena not anticipated based on preliminary analyses. The other two models were stable over the operating range tested. When the flutter did occur, an expanded experimental and analytical effort was undertaken by NASA to gain an understanding of the phenomena. This paper describes the experiment, summarizes the experimental results, presents analytical results, and correlates experimental and analytical results for the SR-5 model.

APPARATUS AND PROCEDURES

Wind Tunnel

The experiment was conducted in the NASA Lewis 8- by 6-Foot Supersonic Wind Tunnel. This tunnel (6), has a 2.44-m (8-ft) high by 1.83-m (6-ft) wide rectangular test section, which is perforated to minimize model/wall interactions in the transonic speed range. The tunnel was run in an open circuit mode where air is drawn in upstream and is exhausted to atmosphere downstream of the test section. The test section Mach number was varied from 0.36 to 0.85. Air flow density and Mach Number cannot be varied independently in this facility.

Propeller Test Rig

The Lewis 746-W (1000 hp) test rig was used for this experiment. The rig was strut supported from the ceiling in the tunnel transonic test section, with the propeller thrust axis alined with the tunnel centerline (fig. 1). It was powered by a 0.15-m (6-in) turbine using a 3103-kPa (450-psi) air supply, which could be heated to 93° C (200° F).

Turboprop Model

The turboprop model, designated SR-5, is an approximate 1/7 scale, advanced propeller configuration consisting of a steel hub, an aluminum spinner, and 10 6AL-4V alloy solid titanium blades. Propeller rotation is counterclockwise (as the pilot sits) and the nominal propeller tip diameter is 0.622 m (24.50 in). The hub-blade assembly includes a gear arrangement for manually setting the blade pitch angle and for pitch angle sychronization between blades. The blade numbers used in this paper correspond to the number assigned to the hub port in which the blade was installed. Hub ports were numbered sequentially from 1 to 10 clockwise.

2

Hamilton Standard designed the model for NASA. Design operating conditions for the propeller model at the Lewis 8- by 6-Foot Supersonic Wind Tunnel are shown in table I. Figure 2 is a photograph showing the SR-5 blade in plan and edge views. The SR-5 blade sweep is incorporated on a helix and the geometric tip sweep, as defined in figure 3, is 60°.

Blade thickness ratio, chord ratio, lift coefficient (camber), and twist angle along the blade span are shown in figure 4. Note that the blade root sections have NACA 65-series airfoils with circular arc mean line, while the outer sections are NACA 16-series airfoils (7). Between these sections a transition region exists. The blades were fabricated with the camber distribution shown, but were fabricated with pretwist to give the twist distribution shown, when at the design rotational speed. Blade characteristics, shown in figure 4, are defined in a plane inclined at the slope of the local blade streamlines.

In addition to the 10-bladed configuration, some tests were made with a 5-bladed configuration by removing every other blade from the hub. A two-bladed configuration was also tested by removing all but two opposite blades. The empty blade ports in the hub were filled and aerodynamically faired smooth for both the two and five-bladed tests.

Instrumentation

Foil strain gages on the cambered (suction) surfaces of selected blades were used to measure stresses due to flexure and torsion. The installation of strain gages on a fully-gaged blade is shown in figure 5. Four uniaxial flexure gages and one biaxial shear gage on the camber surface, plus a uniaxial flexure gage on the blade shank at the trailing edge fillet, were used. These gages were placed at the maximum stress locations for the first four vibration modes of the blade as determined by finite element analysis. All blades were not fully instrumented for these tests, but gages used correspond to locations shown in figure 5. The number of strain gages used was limited by the number of channels available on a rotary transformer device used to transmit electrical signals across the rotor.

The experiment was started with the 10-blade strain gage installation shown in figure 6(a). Blade 1 was fully instrumented and blade 6 partially instrumented. When the flutter was encountered, a significant stress difference was found between the two strain-gaged blades. The 10-blade strain gage installation was then revised to monitor blades one through nine, inclusive with strain gage 1 which was the best indicator of the flutter condition. The blades with the maximum observed stress amplitudes were gaged for the 5-blade configuration as shown in figure 6(b). The 2-blade strain gage installation, with blades 1 and 6, is shown in figure 6(a).

Strain gage vibratory signals were monitored during testing in the time domain with oscilloscopes, and in the frequency domain with a Fast Fourier Transform (FFT) digital signal analyzer. All strain gage data were also recorded on magnetic tape. In addition, a one-per-revolution signal from the model was recorded and was available for control room use. The oscilloscope sweep was triggered with the one-per-revolution speed signal, making it possible to determine if a strain gage signal was a nonintegral order of rotational speed, typical of flutter.

Several techniques were used to provide additional information during flutter testing. Two stroboscopic photographic systems were utilized. A video system was used to monitor and record propeller vibratory motions. To detect aerodynamic shock waves on the blades, a 35-mm camera system was used to record tuft patterns and surface paint flow patterns (8) on the rotating propeller blades. A traversing, steady-state, total-pressure probe was also used to give indication of the presence of shocks by measurement of radial pressure profiles downstream of the propeller.

Test Procedures

The model rotational speed, at a fixed blade pitch angle and tunnel Mach number, was incrementally increased until an operating limit (blade stress, rotational speed, rig power, or vibration) was reached. Maximum allowable rotational speeds was 9000 rpm.

An inclinometer was used to set the blade pitch angle at the 0.73 R location (β_{ref}) prior to tunnel start-up. The blade-hub gear arrangement, mentioned earlier, allowed a single blade to be used for this procedure.

EXPERIMENTAL RESULTS

Before presenting the experimental results, some information about the SR-5 blade's dynamic characteristics, as well as the concept of nodal diameter, interblade phase angle, and traveling waves, will be useful.

A finite element analysis was used to determine the SR-5 blade's natural frequencies versus rotational speed, as shown in figure 7. The average natural frequencies of the 10 blades, measured in air at nonrotating conditions, are also indicated. Analysis and holographic photos show the first mode to be primarily flatwise bending.

The concepts of traveling waves, interblade phase angles, and nodal diameters are commonly used to describe the system flutter mode characteristics of a flexible blade-disc assembly. A tuned blade system flutter mode can be characterized by a traveling wave involving a single interblade phase angle, and a nodal diameter pattern (the number of equally spaced node lines lying along the diameters of the rotor). The number of blades on the rotor N, the number of nodal diameters r, and the interblade phase angles σ_r are related by the equation

$$\sigma_r = 360 \ r/N$$

where

$$r = 0, 1, 2, \ldots, N-1.$$

Interblade phase angles between $0°$ and $180°$ produce forward (in the direction of rotation) traveling waves, while phase angles between $181°$ and $359°$ (or $-179°$ and $-1°$ degrees) produce backward traveling waves.

The variables of the test were number of blades, blade pitch angle (β_{ref}), free stream Mach number, and rotational speed. Mach numbers from 0.36 to 0.85 and blade pitch angles from $47°$ to $75°$ were investigated. The instability occurred only at Mach numbers of 0.6 and greater over the full blade angle range. At large blade angles, a rig power limit restricted the

4

rotational speed that could be reached. A summary of the flutter data for the 10-blade, 5-blade, and 2-blade configurations is shown in figure 8. Here the rotational speed, blade angle, and Mach number at which the flutter occurred are defined for each configuration. It was noticed during testing that the onset of the flutter condition could be correlated to the blade tip relative Mach number. Lines of constant tip relative Mach number are included in figure 8. It can be seen that for the 10-blade configuration and the 5-blade configuration, the instability developed at tip relative Mach numbers of about 0.95 and 1.10, respectively. The tip relative Mach number of the 2-blade configuration was higher yet and will be discussed later. At a particular Mach number, the rotational speed at which the instability occurred was affected by blade pitch angle. As the pitch angle was increased, the instability occurred at lower rotational speed. Note that decreasing the number of blades increased the operating region, indicating that aerodynamic cascade effects have a destabilizing influence on flutter.

The flutter that was experienced with the SR-5 propeller blades had distinctive qualities that could be identified from the blade strain gage signals. The first indication of the instability was low amplitude vibratory gage signals. For each blade these were at a slightly different, nonintegral order, single frequency, near the expected frequency of the first blade mode. As rotational speed was increased, blade-to-blade coupling developed. This was characterized by a predominant and coherent interblade phase angle and a common frequency for all the blades. When the blades were totally coupled, the stresses grew rapidly, reaching operational limits with a slight increase in rotational speed. Thus, the phenomena was characterized by an "explosive" growth of stress amplitude, at a nonintegral order single frequency, near the expected frequency of the first blade mode.

The very rapid increase of stress amplitude is illustrated in figure 9(a) and (b) for two test conditions of the 10-blade configuration. These figures present the peak stress amplitude of gage 1 for blade one as a function of rotational speed. Stress hysteresis is evident in these plots: The speed at which the stress starts to grow is slightly higher then the speed at which the stress subsides. The amount of hysteresis present varies for the different test conditions. This may be related to the rate of change of rotational speed that the model operator used when the rapid rise of stress occurred.

The observed stress signals for the 10-, 5-, and 2-blade configurations confirmed the previous observation that aerodynamic cascade effects were significant for the 10- and 5-blade configurations, but not for the 2-blade configuration. With two-blades, the explosive growth of stress did not occur. The flutter points shown on figure 8 for the 2-blade case are for this condition, whereas the 5- and 10-blade data are at the explosive stage.

Although the stress levels for the 2-blade configuration were low during flutter, an interesting observation will be noted. During flutter, two simulationeous frequencies differing by 14 Hz occurred (table II) on each blade. The interblade phase angle for the lower frequency was about $180°$, while that for the higher frequency was about $0°$. Thus, a symmetric and asymmetric system mode appeared simultaneously. This may be attributed to the variable moment of inertia property of a two-blade propeller with respect to a fixed diametral axis in the propeller plane of rotation or may be due to unidentical blade properties.

5

The instability did not degrade the propeller performance as might be expected if shock waves were present. Plots made of advance ratio J versus power coefficient C_p were smooth and continuous at all Mach numbers until operation was stopped by the instability. It will also be noted that no shock waves could be detected on the blades with the flow visualization and pressure probe techniques, described under the Instrumentation section.

The measured flutter frequencies are shown in figure 10 and are close to the calculated first mode frequencies of figure 7. Thus, for all propeller configurations and test conditions, the first vibration mode of the blade was predominant during flutter.

The blade peak stress amplitudes during flutter for a 10-blade configuration are compared in figure 11. A large variation in stress amplitudes among the blades can be seen. Although not shown, the blade-to-blade stress variation for the 5-blade configuration was not as great. The stress variation of the 10-blade propeller may be attributed to manufacturing variations, resulting in unidentical blade properties (mistuning). In fact, based on measured frequencies of the blades at nonrotating conditions, the 5-blade was better tuned than the 10-blade configuration.

The interblade phase angle during flutter for the 10- and 5-blade configurations are shown in figures 12(a) and (b). The phase angle of the blades are shown relative to blade 1. Scatter in the 10-blade data (fig. 12a) is attributed to mistuning. The interblade phase angle data indicate that both the 5 and 10-blade configurations responded as a two-nodal-diameter forward traveling wave system. Using the equation given on page 8, the nominal interblade phase angle was 144° for the 5-blade, and about 72° for the 10-blade configurations. The effects of frequency mistuning observed here is in qualitative agreement with the analytical results presented in (9).

The concepts of interblade phase angle and nodal diameter, discussed earlier, are characteristics of blade system flutter. We will now address the interaction of the bending and torsion motions on an individual blade during flutter. A coupling of bending and torsion vibrations, with torsion leading the bending, is generally characteristic of classical flutter found in practice. The phase angle between bending and torsion motion on each blade will be designated herein as intrablade phase angle, in contrast to the interblade phase angle described earlier.

An intrablade coupling was also found to be present during flutter. This is illustrated for the 5- and 10-blade configuration in table III. Shown is the phase relationship of strain gages 3 and 5, relative to strain gage 1 on blade 1. Strain gages 3 and 5, located near the tip, are sensitive to torsional motion, while gage 1, located near the root, is sensitive to flatwise flexural motion. From table II, it can be seen that the tip motion is leading the motion of the root by about 20 to 25° for most of the test points. The only exception was for data obtained during a short excursion into the flutter region, farther than usual, in a windmilling condition. This resulted in high stresses and a much larger phase angle between the blade tip and blade root motions. The intrablade phase angles for the 2-blade configuration are shown in table II. These values were slightly higher than those of the 5- and 10-blade configurations.

The phase angle data was obtained by computing a time-averaged cross-power spectra of the strain gage signals. Included in this was a computation of the coherence function. For every computation made to determine the intrablade phase angle, the value of the coherence function was always unity, indicating a highly coherent phase angle. The data show the blade flutter consists of a coupled bending and torsional motion, with the torsion leading the bending by a fixed phase angle. Furthermore, the coupled bending-torsional motion was observed from video pictures obtained while the blades were in flutter.

ANALYSIS

As described under experimental results, the flutter encountered in testing the SR-5 propeller model appeared to be a classical type involving coupling betweeen bending and torsional motions of the blades. However, this flutter was predicted to occur at a much higher speed than measured by an analysis in which two-dimensional, unsteady, isolated subsonic airfoil theory was used. The poor correlation between the experimental and analytical results suggested that an improved analysis was required. The purpose of the analytical investigation presented herein is to provide a basis for such an analysis and to explain the observed flutter phenomena by correlating the experimental and theoretical results.

The poor correlation between the measured and predicted flutter speed was thought to be due to one or more of the following factors: transonic effects, stall effects, mistuning effects, blade geometric structural nonlinearities, and sweep and/or aerodynamic cascade effects. Transonic flow induced flutter was suspected since the tip relative Mach number at the onset of flutter was near unity, but was tentatively ruled out for the SR-5 blades since no shock waves could be located experimentally. Stall flutter also was suspected but was ruled out since the flutter occurred during windmilling conditions and at other conditions of low incidence angles to the blades. Based on helicopter and wind turbine dynamics experience, it was believed that the effect of geometric structural nonlinearities on the flutter of the SR-5 blades was of second-order. It was shown in (9) that blade-mistuning always retards the onset of flutter. The experimental flutter data obtained by testing the 2-, 5-, and 10-blade configurations showed that aerodynamic cascade effects strongly influenced the flutter onset conditions. These observations indicated that a starting point for the improved analysis was to evaluate aerodynamic cascade effects including blade sweep. To accomplish this, two simplified models with increased complexity are considered. The first model is designated as a hypothetical model and the second one is designated as a beam model. These models, their specific objectives, and their analytical results are described in this section.

Hypothetical Model and Results

The main purpose of the hypothetical model was to assess the importance of blade sweep and aerodynamic cascade effects on the flutter of the SR-5 propeller. For the purpose of simplicity, a nonrotating model with 10 radial, equally-spaced, identical, uniform, cantilevered blades, with no twist and stagger, was treated. The blade elastic axis was swept at a constant angle measured from an axis perpendicular to the flow direction. Only the pure bending motion in the direction perpendicular to the chord was considered. This model was kept in a uniform subsonic flow. For simplicity, it was as-

7

sumed that the unsteady cascade aerodynamic load was the same along the entire blade span of the model. To accomplish this, the gap to chord ratio of the three-quarter radius station was used as a representative value for the entire blade. With these assumptions, this model is an extended version of the fixed-wing model used by Cunningham (10) for studying the effects of sweep on pure-bending flutter of a cantilever wing. The blade was constrained, as in (10), to have one generalized coordinate by assuming a single mode for bending motion. Then, the main difference between the present blade model and the fixed-wing model is in the aerodynamics. In the present model, aerodynamic cascade effects are included.

The two-dimensional subsonic unsteady cascade aerodynamic loads for an unswept blade were calculated by using the theory presented in 11. The corresponding loads for the swept blade are obtained by applying similarity laws, as discussed in 12 and 13, for the case of a fixed-swept wing.

Since the blades are tuned, the 10-blade cascade has 10 uncoupled inter-blade phase angle modes, with a constant phase angle between adjacent blades. The possible phase angles are $\sigma_r = 360\ r/10$ $(r = 0, 1, 2,..., 9)$. Since the stagger angle is zero for the hypothetical model, the aerodynamic loads for $\sigma_r = 36°$, $72°$, $108°$, $144°$ are the same as those for $\sigma_r = 324°$, $288°$, $252°$, $216°$, respectively. Furthermore, cascade flutter usually does not occur in the zero interblade phase angle mode. It is, therefore, sufficient to consider only $\sigma_r = 36°$, $72°$, $108°$, $144°$, $180°$ interblade phase angle modes for the hypothetical model.

The results of the hypothetical model with no structural damping are presented in figure 13. The abscissa is a sweep parameter $\gamma = \tan \Lambda/(1/b)$ where Λ is the blade sweep angle, 1 is the length of the blade measured along the elastic axis, and b is the semichord measured perpendicular to the elastic axis. Positive γ indicates sweepback. The ordinate is an intertial parameter $\mu\ [1-\omega_h/\omega)^2]$, where μ is the nondimensional mass ratio $m/\pi\rho b^2$, m is the mass per unit length of the blade along the elastic axis, ρ is the air density, and ω_h and ω are the blade uncoupled bending frequency and flutter frequency, respectively. Along the boundary curves the reduced frequency is varied.

The same parameters are used as in 10. In figure 13, the ordinate along the boundary curves may be considered as the smallest value of the mass ratio, μ, which can be had, and allow single-degree bending flutter (the limiting value of μ is actually associated with the condition $\omega_h/\omega = 0$). The abscissa defines the lowest value of γ, just as the ordinate defines the lowest value of μ, and these are transitional values. Thus, to the right of a boundary curve the blade is unstable, and to the left of the boundary it is stable. The flutter boundaries for the interblade phase angles $\sigma_r = 36°$, $72°$, $108°$, $144°$, and $180°$ are shown. Also included in the figure are the flutter boundaries of one-blade, with isolated airfoil theory at Mach numbers $M = 0$ and 0.7. These isolated airfoil theory boundaries are the same as those presented in (10). The sweep and the flutter parameters for the SR-5 wind tunnel model are also shown. It should be mentioned that these parameters are estimated.

Several interesting observations follow from figure 13. First, comparing the isolated airfoil theory boundaries for $M = 0$ and $M \cos \Lambda = 0.7$, compressible flow has a very strong destabilizing effect on single-degree bending

flutter. Particularly, for a given value of the ordinate, the value of the sweep parameter γ at the flutter condition is much lower for compressible flow then for incompressible flow. Second, comparing the isolated airfoil and cascade airfoil theory flutter boundaries for $M \cos \Lambda = 0.7$, cascade effects on flutter may be adverse or favorable, depending on the range of sweep and mass ratio parameters as well as interblade phase angles. For $\sigma_r = 36°$ and $72°$, the cascade effects are adverse on flutter; for $\sigma_r = 108°$, $144°$, and $180°$, the cascade effects are favorable if $[\mu (1 - \omega_h^2/\omega^2)] > 90$ approximately, but are unfavorable if $[\mu (1 - \omega_h^2/\omega^2)] < 90$. Third, the estimated parameters of SR-5 lie close to the two nodal diameter ($\sigma_r = 72°$) flutter boundary. Fourth, increasing the blade sweep angle and/or decreasing the structural aspect ratio has a destabilizing effect on single-degree bending flutter. The qualitative observations that the aerodynamic cascade effects are destabilizing and that the two-nodal diameter mode is the most critical one are in agreement with the experimental results presented earlier. It should be noted that although coupled bending-torsion flutter is not studied with the hypothetical model, based on the results presented in 10, it is expected the parameters affecting the uncoupled bending flutter boundaries have a similar qualitative effect on coupled bending-torsion flutter over a significant range of the parameters. Hence, it is concluded that (1) aerodynamic cascade effects on flutter are significantly unfavorable, and (2) a single-degree-of-freedom bending flutter is theoretically possible for sufficiently large values of blade sweep in the presence of cascade aerodynamics. The next step is to calculate the flutter boundary of the SR-5 configuration with a more realistic structural model.

Beam Model and Results

The main purpose of the beam model was to calculate the flutter boundary of the SR-5 wind tunnel model. To obtain the results expeditiously, the beam model developed, (14), for studying cascade flutter was modified to account for blade sweep in an approximate manner. The blade sweep of the SR-5 blades varies along the blade span. To minimize algebraic complexity in deriving the equations of motion with varying blade sweep, the sweep angle of the beam model was kept constant. A schematic of this model is shown in figure 14. Furthermore, some higher order elastic and inertial terms associated with blade sweep and steady-state aerodynamic loads were neglected. The unsteady cascade aerodynamic loads for the swept blade were obtained by applying the same theory and similarity laws to account for blade sweep that were used for the hypothetical model. The blade twist, chord, sectional properties, reduced frequency, and Mach number were allowed to vary along the blade span. All the possible interblade phase angle modes were included. As in (14), the blade deflections were expressed in a traveling wave form in terms of a set of generalized coordinates, which are associated with nonrotating uncoupled beam modes in pure bending and torsion. The analysis was performed using two modes in each the plane of rotation, the plane perpendicular to the plane of rotation, and torsion. Since the blades are assumed identical, the total number of coupled degrees of freedom for the rotor is six. Thus, the stability analysis consists of 10 separate iterative eigenvalue solutions (one for each interblade phase angle), each consisting of six degrees of freedom. The flutter boundary for the SR-5 model was calculated by using the iterative procedure described in 14.

9

The flutter boundary of the SR-5 for the 10-blade configuration, as calculated with the beam model, is evaluated in figure 15 together with the experimental results. The representative value assumed for the blade sweep is 30°. The other parameters are listed in the figure. Comparison of the results in figure 15 show that the calcualted rotor speed for flutter decreases with an increase in free-stream Mach number. This trend is in agreement with the data. For tunnel Mach numbers in the range of 0.65 to 0.75, the calculated rotational speeds for flutter are less than those measured. This conservative prediction of rotor speed may be due to the following factors: (1) the limitations of the beam model and the approximate sweep assumption, (2) the assumption that the structural damping is zero in the analysis, (3) the limitations of two-dimensional unsteady cascade theory, and (4) the assumption that the steady state aerodynamic loading can be neglected, and (5) nonlinear transonic effects. The first and last factors are probably the most significant. Some efforts are being made to improve the structural model and to account for unsteady transonic effects using isolated airfoil theory. It is to be noted that in spite of the assumptions and simplifications made in the analysis, the correlation between experiment and theory is suprisingly good.

CONCLUSIONS

An experimental and analytical study was performed to investigate a flutter pheonomena encountered during wind tunnel testing of an advanced propeller having highly swept, flexible blades. The analysis was based on simplified aerodynamic and structural models. Based on the results of these studies, the following conclusions are reached:

1. The flutter was of a classical type involving coupling between blade bending and torsion motions.

2. The flutter occurred in a two-nodal diameter forward traveling wave mode.

3. The blade-to-blade stress amplitudes varied during flutter, but the most and least active blades remained the same during the experiment. This variation is attributed to blade frequency mistuning, particularly in the 10-blade configuration.

4. Both experiment and theory show that aerodynamic cascade effects have a strong destabilizing influence on the flutter boundary.

5. As in the case of fixed wings, analysis shows that sweep has a destabilizing effect on classical flutter of propellers.

6. Analytical results obtained with a simplified beam model that includes sweep and aerodynamic cascade effects show good correlation with the flutter data.

APPENDIX — SYMBOLS

b	Blade semichord
C_L	Lift coefficient
C_p	Power coefficient $= p/\rho n^3 D^5$
D	Blade tip diameter
J	Advanced ratio, V/nD
l	Length of blade measured along the elastic axis
m	Mass per unit length of the blade along the elastic axis
n	Rotational speed, revolutions per second
N	Number of blades in rotor assembly
P	Order of vibration due to rotational speed (i.e., the number of excitations per revolution)
r	Radius; Nodal diameter index
R	Blade tip radius
t	Blade thickness
V	Free-stream velocity
'REF	Blade pitch angle (between the blade chord and the plane of rotation) at the 0.73 R location
θ	Blade twist angle
Λ	Sweep angle, positive for sweepback
μ	Nondimensional mass ratio, $m/\pi\rho b^2$
ρ	Air density
σ_r	Interblade phase angle, degrees
ω	Flutter frequency
ω_h	Blade uncoupled bending frequency
γ	Sweep parameter, $\gamma = \tan \Lambda/(l/b)$

REFERENCES

1. L. H. G. Sterne, "Spinning Tests on Fluttering Propellers," British A. R. C., R & M No. 2022, August 1945.

2. H. G. Ewing, J. Kettlewell and B. A. Gaukroger, "Comparative Flutter Tests on Two, Three, Four, and Five-Blade Propellers," British A. R. C., R & M No. 2634, 1952.

3. J. E. Baker, "The Effects of Various Parameters, Including Mach Number, On-Propeller-Blade Flutter With Emphasis on Stall-Flutter," National Advisory Committee for Aeronautics, NACA TN 3357, January 1955.

4. H. H. Hubbard, M. F. Burgess and M. A. Sylvester, "Flutter of Thin Propeller Blades, Including Effects of Mach Number Structural Damping, and Vibratory-Stress Measurements Near the Flutter Boundaries, National Advisory Committee for Aeronautics, NACA TN 3707, June 1956.

5. J. F. Dugan, B. A. Miller, E. J. Grabear and D. A. Sagerser, "The NASA High-Speed Turboprop Program, National Aeronautics and Space Administration, NASA TM-81561, October 1980.

6. R. J. Swallow and R. A. Aiello, "NASA Lewis 8 by 6 Foot Supersonic Wind Tunnel," National Aeronautics and Space Administration, NASA TM X-71542, May 19

7. I. H. Abott and A. E. vonDoenhoff, "Theory of Wing Sections." New York, N. Y.: Dover Publications, 1959.

8. G. A. Mitchell and D. C. Mikkelson, "Summary and Recent Results from the NASA Advanced High-Speed Propeller Research Program, National Aeronautics and Space Administration, NASA TM 82891, June 1982.

9. K. R. V. Kaza and R. E. Kielb, "Effects of Mistuning on Bending-Torsion Flutter and Response of a Cascade in Incompressible Flow," AIAA Paper No. 81-0532, August 1982, pp. 1120-1127.

10. H. J. Cunningham, "Analysis of Pure-Bending Flutter of a Cantilever Swept Wing and Its Relation to Bending-Torsion Flutter, National Advisory Committee for Aeronautics, NACA TN 2461, September 1951.

11. S. N. Smith, "Discrete Frequency Sound Generation in Axial Flow Turbomachines, British A. R. C., R & M No. 3709, 1972.

12. J. G. Barmby, H. J. Cunningham and I. E. Garrick, "Study of Effects of Sweep on the Flutter of Cantilever Wings," National Advisory Committee for Aeronautics NACA TN 2121, June 1950.

13. R. L. Bisplinghoff, H. Ashley and R. Halfman, "Aeroelasticity." Reading, MA: Addision-Wesley Publishing Co., 1955.

14. K. R. V. Kaza and R. E. Kielb, "Coupled Bending-Bending-Torsion Flutter of a Mistuned Cascade with Nonuniform Blades," AIAA Paper No. 82-0726, 1982.

TABLE 1 - SR-5 MODEL DESIGN OPERATING CONDITIONS AT THE
LEWIS 8x6-FOOT SUPERSONIC WIND TUNNEL

```
Mach number . . . . . . . . . . . . . . . . . . . . . . . . . . 0.8

Static pressure, kN/m² (psf) . . . . . . . . . . . . . . . . 76.6 (1601)

Static temperature, K(°R) . . . . . . . . . . . . . . . . . 292 (525)

Rotational speed, rpm . . . . . . . . . . . . . . . . . . . . . . 7950

Tip speed, m/sec (ft/sec) . . . . . . . . . . . . . . . . . 259 (850)

Power, kW (hp) . . . . . . . . . . . . . . . . . . . . . . . 388 (520)

Thrust, N (lb) . . . . . . . . . . . . . . . . . . . . . . . 1112 (250)

Blɛ pitch angle, βref, deg . . . . . . . . . . . . . . . . . . . 61.6
```

TABLE 2 - TWO-BLADE CONFIGURATION TYPICAL PHASE RELATIONSHIP
DATA AT FLUTTER CONDITIONS

Data point	Mach number (tunnel)	Blade angle β_{ref} deg	Rotational frequency, Hz	Flutter frequency Hz	Intrablade phase angles, deg		Interblade phase angles, deg	Coherence
					gage 1 versus gage 3	gage 1 versus gage 5	blade 1 versus blade 6	
6681	.7	65.7	146	204 218	-40.1 -37.1	-39.1 -36.3	177.2 4.0	0.93 1.00
6691	.8	65.7	138	198 212	-34.4 -32.5	-35.0 -33.3	177.6 6.0	1.00 .61
6717	.8	67.4	130	192 206	-26.2 -23.0	-29.1 -25.8	175.6 8.7	1.00 .98

TABLE 3 - 5- AND 10-BLADE CONFIGURATION TYPICAL PHASE
RELATIONSHIP DATA AT FLUTTER CONDITIONS

Data point	Mach no. (tunnel)	Blade angle, β_{ref} deg	Rotational frequency Hz	Flutter frequency Hz	Maximum stress (at flutter freq) MPa (ksi)	Intrablade phase angles, deg	
						gage 1 versus gage 3	gage 1 versus gage 5
5-Blade configuration							
7586 7646	0.8 .85	69 69	117 118	182 .80	93.8 (13.6) 74.5 (10.8)	-23.3 -26.0	-25.7 -27.1
10-Blade configuration							
6145 6157 Overspeed	0.6 .75 .775	65.2 65.2 65.2	136 124 174	197 186 237	98.6 (14.3) 100.7 (14.6) 281.3 (40.8)	-20.6 -21.7 -47.7	-23.3 -21.8 -42.2

SURFACE MOTION	TECHNICAL SYSTEMS	RESISTANCE TO MOTION	MECHANISM OF DAMAGE
SOLID GAS	AIR BEARING PLANE TURBINE ENGINE	AIR FRICTION	FLUID EROSION
SOLID LIQUID	HYDRAULIC DRIVES SHIP PIPELINE	VISCOUS FRICTION	CAVITATION EROSION
SOLID SOLID	DRY BEARING WHEEL AND RAIL BRAKES	SOLID FRICTION	WEAR

Figure 1. - Types of surface motion and related subjects.

TRIBOLOGY

THE SCIENCE AND TECHNOLOGY OF INTERACTING SURFACES IN REL-
ATIVE MOTION AND OF ASSOCIATED SUBJECTS AND PRACTICES

| ADHESION | FRICTION | WEAR | LUBRICATION |

THE SCIENCE AND TECHNOLOGY OF THE TRANSFER OF FORCES FROM
ONE SURFACE TO ANOTHER WHEN THE TWO SURFACES ARE IN REL-
ATIVE MOTION
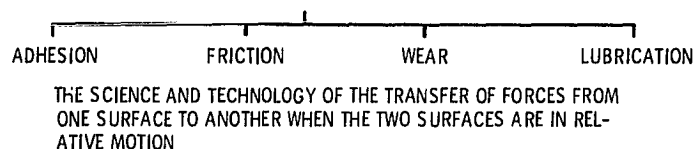
Figure 2. - Definition of tribology.

- MATERIAL LOSSES DUE TO TRIBOLOGY $100 BILLION PER YEAR

(THE NATIONAL COMMISSION ON MATERIALS
POLICY TO THE CONGRESS OF THE U.S.A.
AS REPORTED BY D.W. BALLARD)

- THE TOTAL U.S. COST OF WEAR $100 BILLION

(PROF. RABINOWICZ OF MIT)

- COST OF CORROSION $70 BILLION
  COST OF WEAR $20 BILLION

(NATIONAL BUREAU OF STANDARDS)

- COST OF WEAR PER YEAR   2/3 THE FUEL COST

(ESTIMATES FOR NAVAL AIRCRAFT AND SHIP)
BY PETERSON

Figure 3. - The economic aspect of tribology.
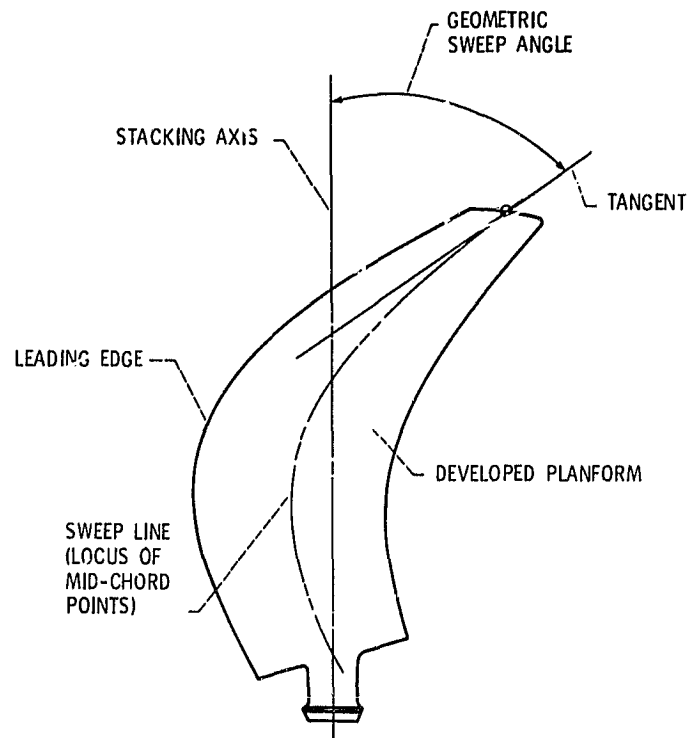
Figure 3. - Geometric tip sweep definition.
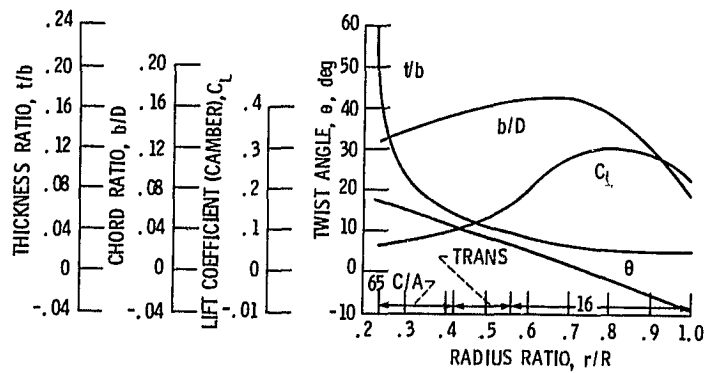
Figure 4. - SR-5 blade characteristics.

BLADE NUMBER

VIEW LOOKING
DOWNSTREAM
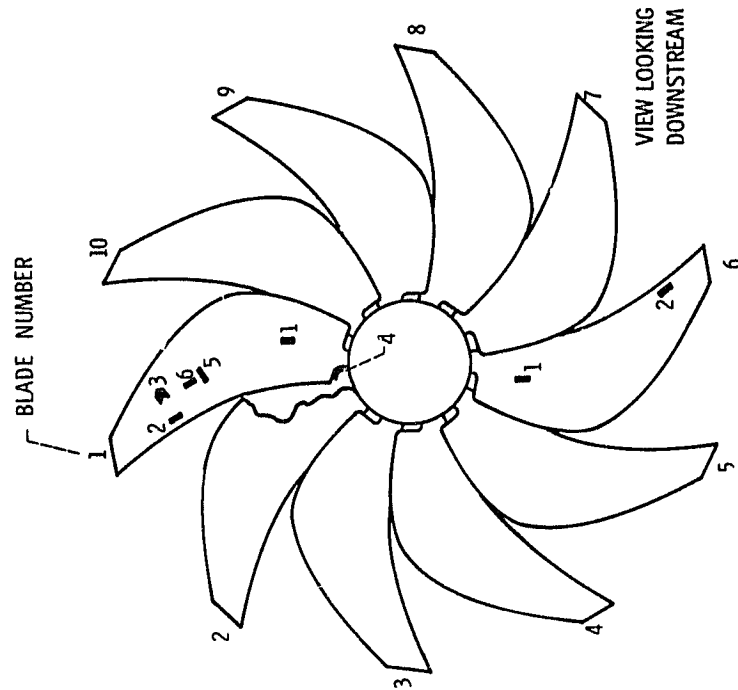
(a) Ten-blade configuration initial installation.

Figure 6. – Blade strain gage installation.

LEADING EDGE

DEVELOPED
PLANFORM
CAMBER SIDE

Ⓧ = GAGE NUMBER

₵ ROTATION

AT SHANK FILLET
ALONG CHORD
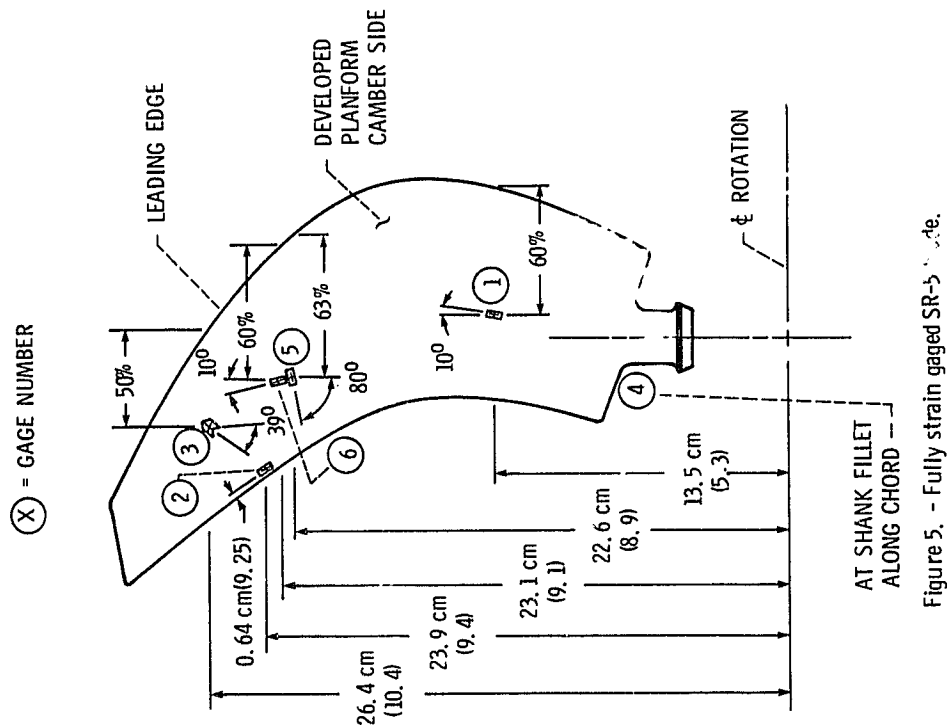
Figure 5. – Fully strain gaged SR-5 blade.
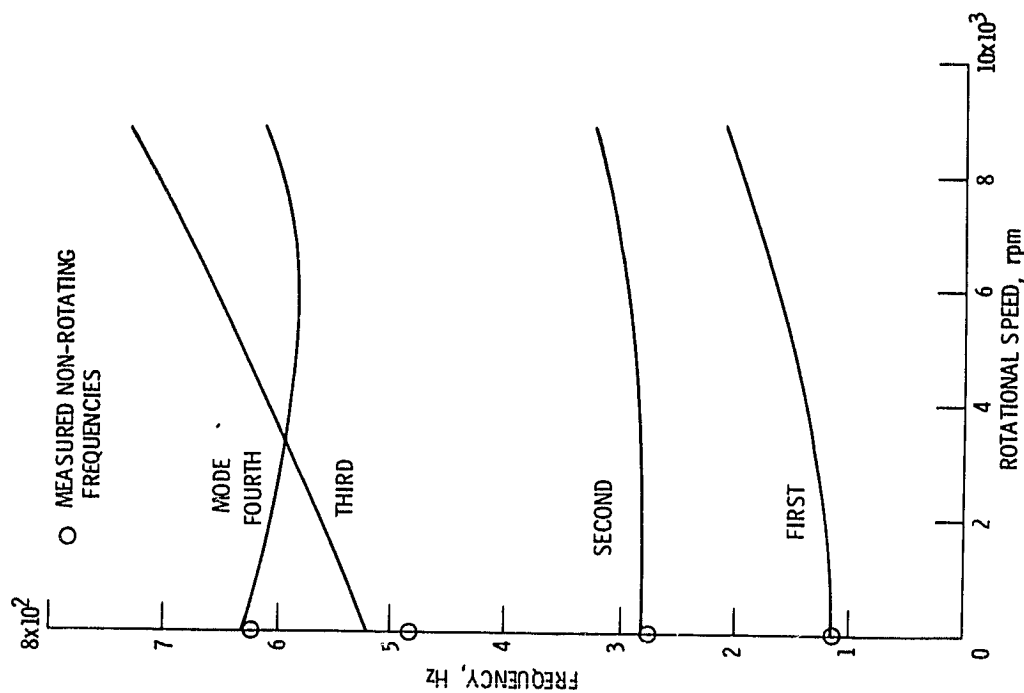
Figure 7. – Analytical natural frequencies as a function of rotational speed, SR-5 blade.

VIEW LOOKING DOWNSTREAM

(b) Five-blade configuration.
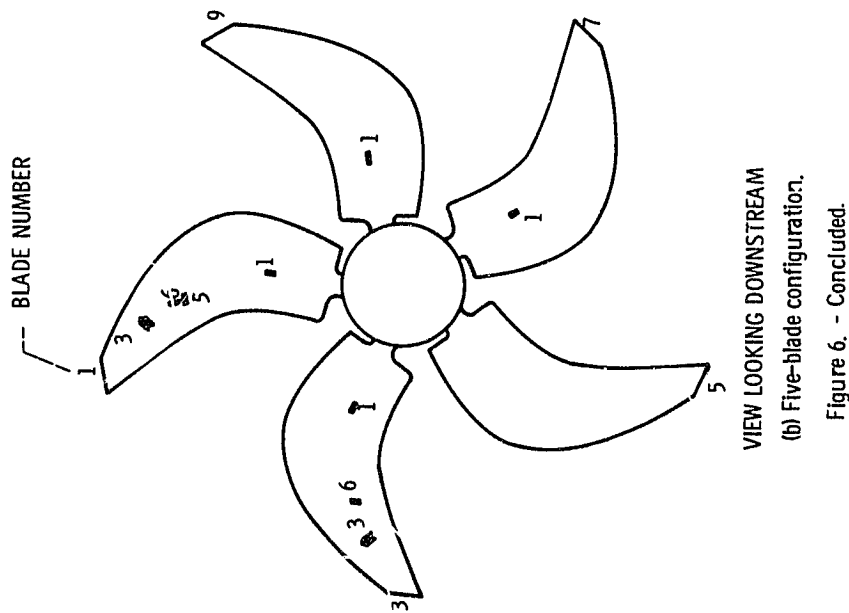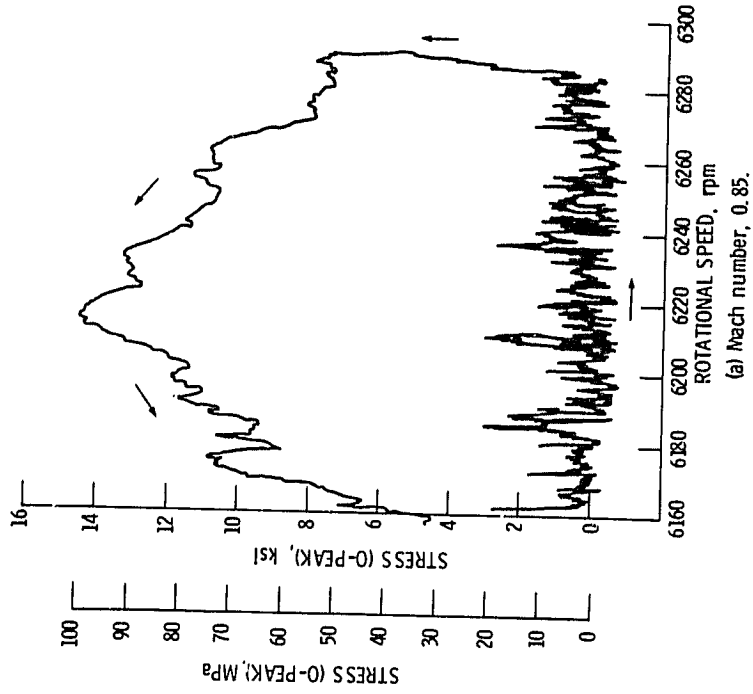
Figure 6. – Concluded.

Figure 9. – Peak stress amplitude vs rotational speed for blade 1, gage 1, β_{ref}, 69.3°.
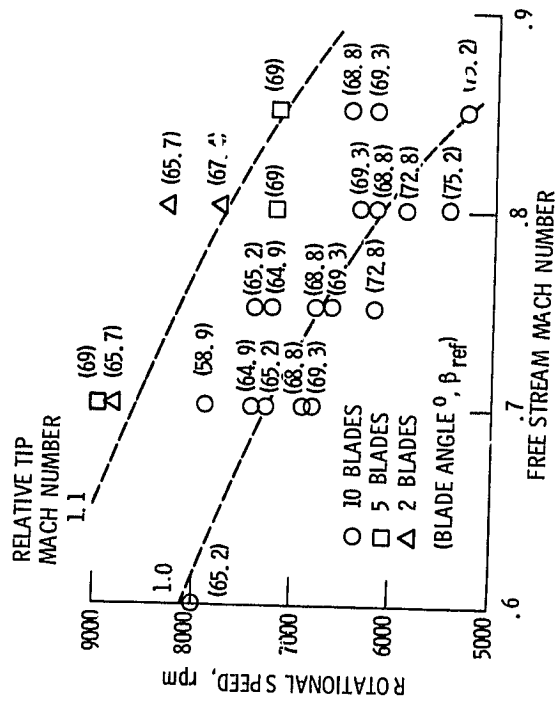
(a) Mach number, 0.85.

Figure 8. – Flutter points as a function of rotational speed, free stream Mach number and blade angle.

Figure 10. - Measured flutter frequency as a function of rotational speed.

(b) Mach number, 0.8.
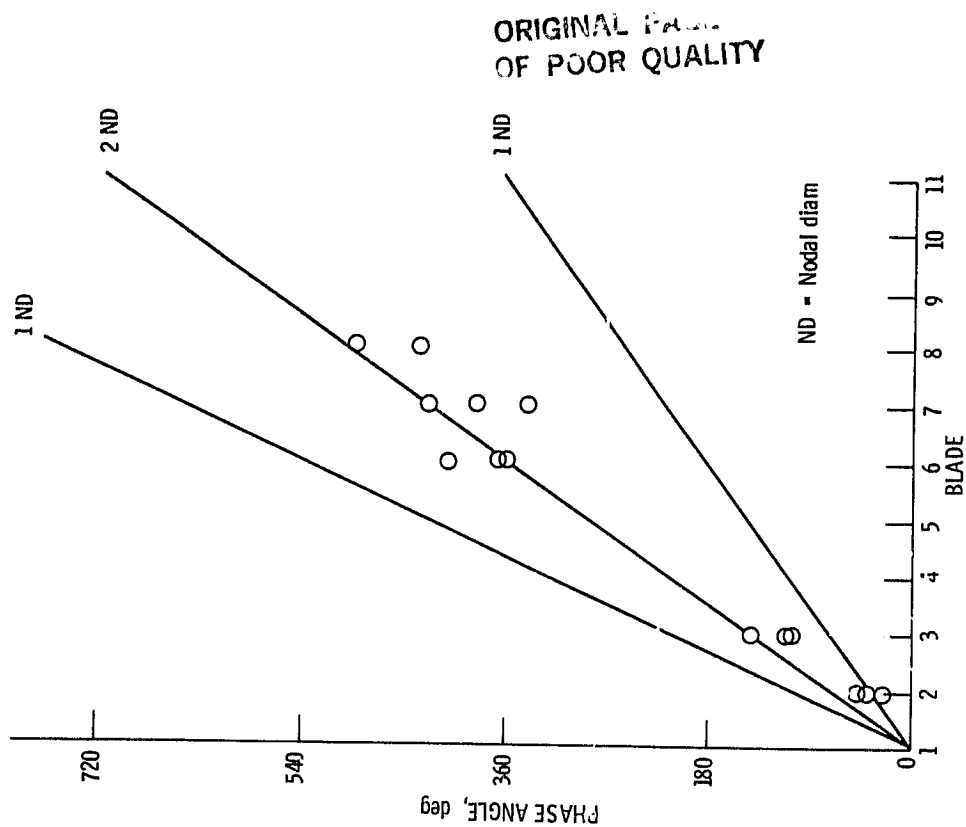
Figure 9. - Concluded.

(a) Ten-blade configuration.

Figure 12. – Interblade phase angles.
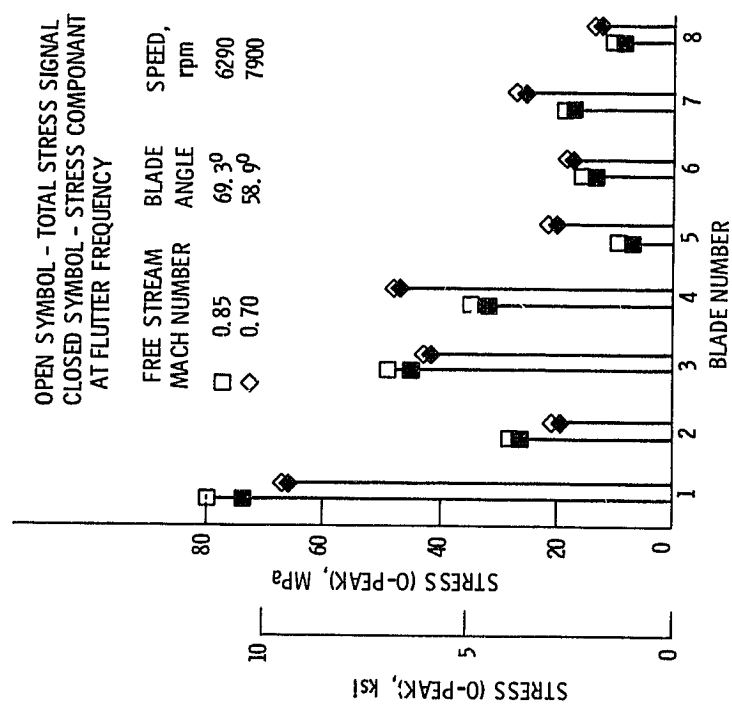
Figure 11. – Typical blade-to-blade variation in stress amplitudes
for 10-blade configuration.
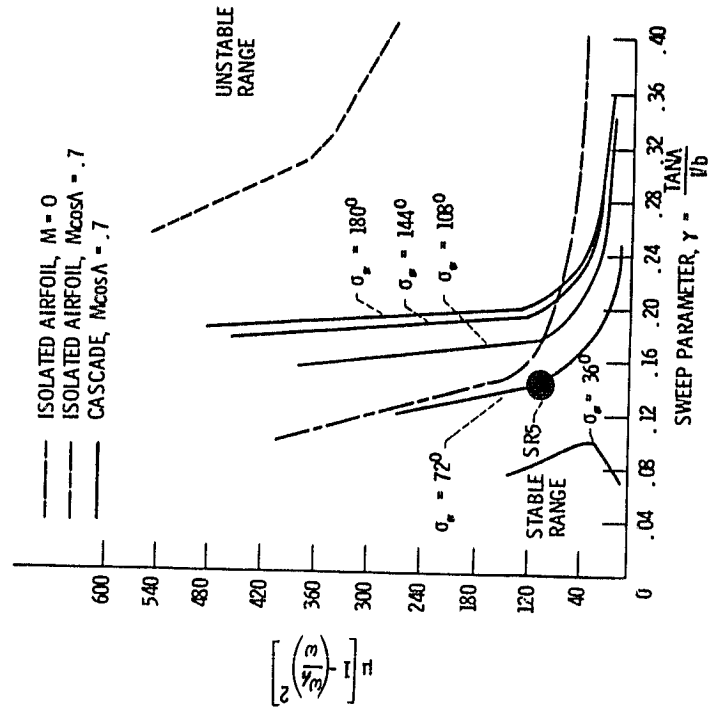
Figure 13. – Hypothetical model results.
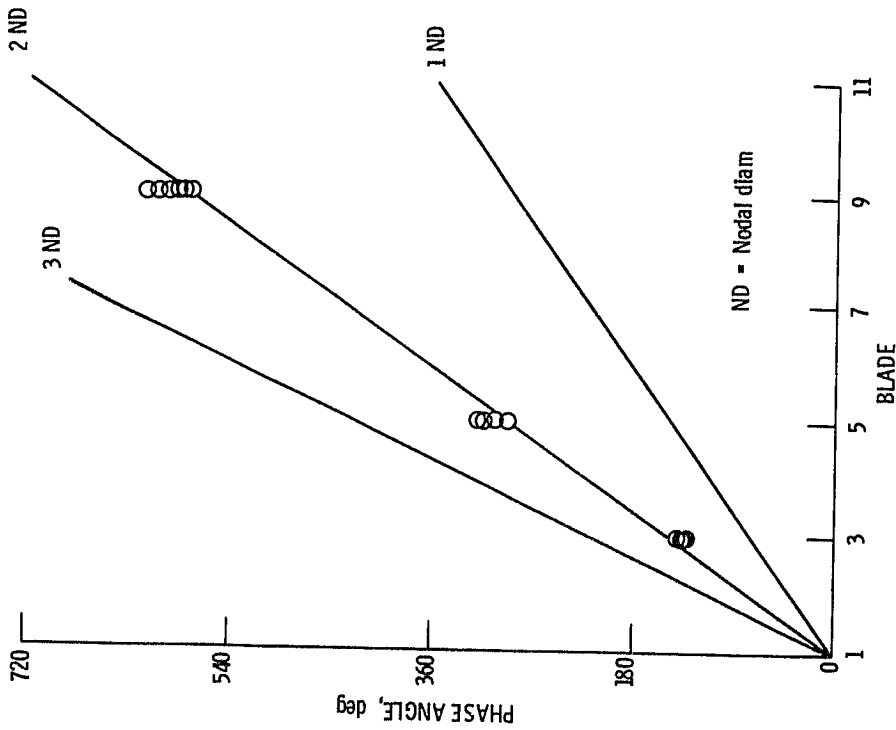
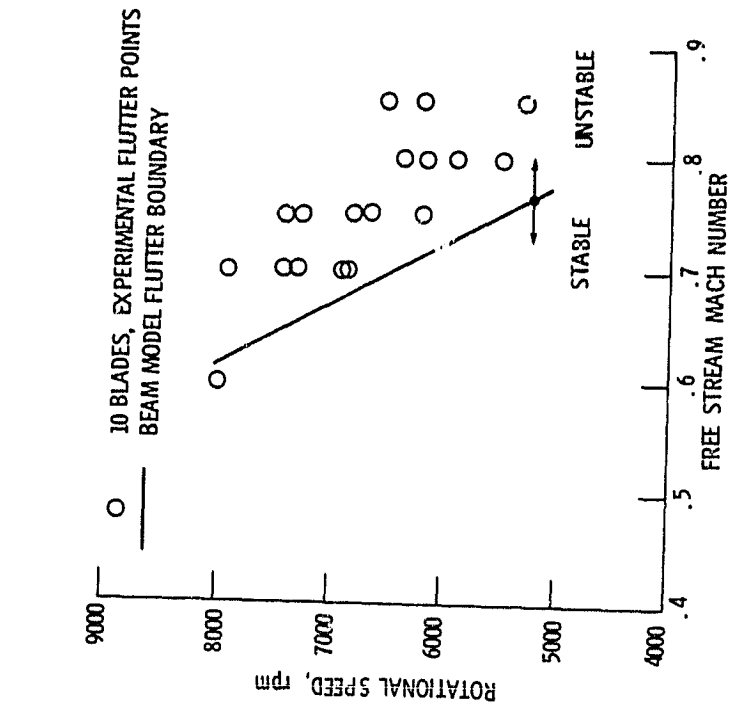
(b) Five-blade configuration.

Figure 12. – Concluded.

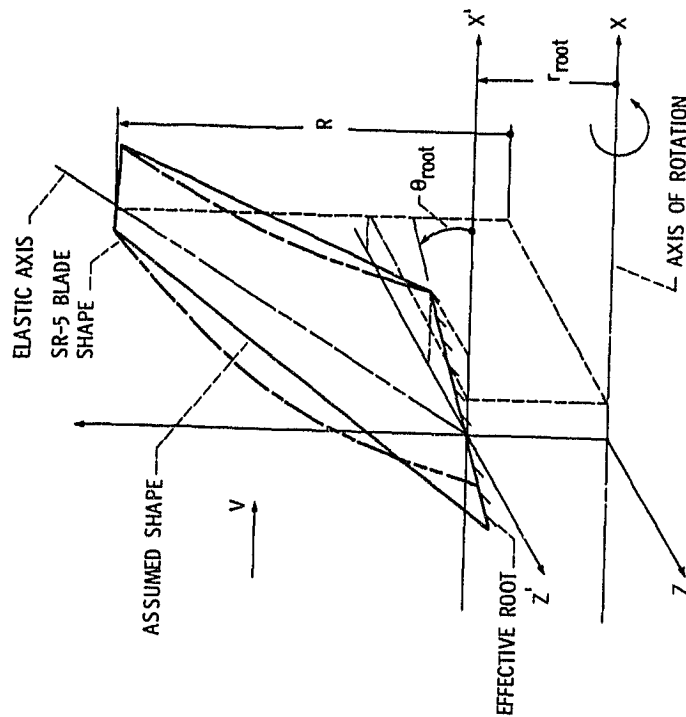Figure 15. - Beam-model flutter boundary and experimental flutter points.

Figure 14. - Swept beam model (schematic).

(a) ARGON-SPUTTER-CLEANED SURFACE.
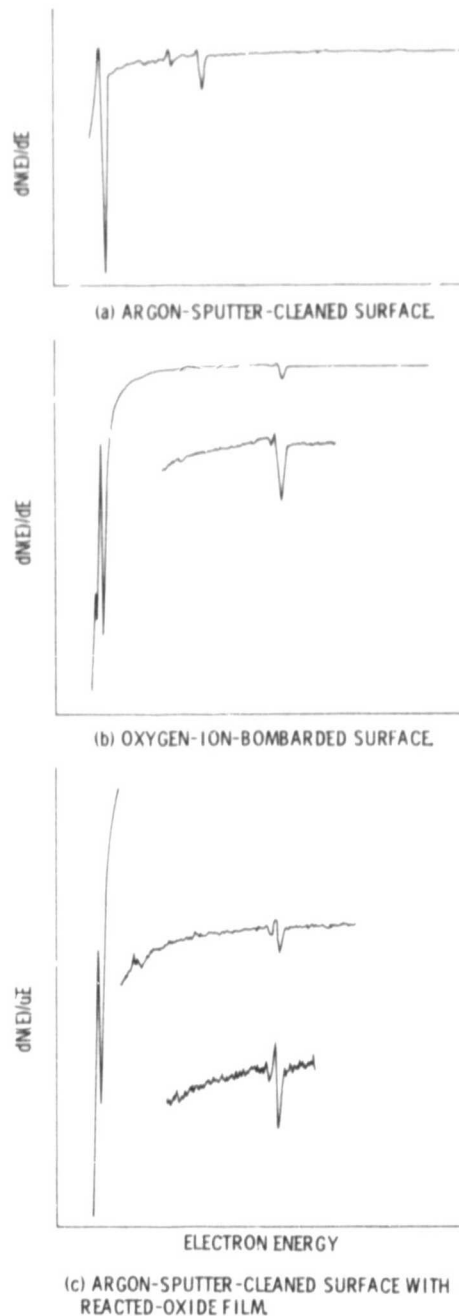
(b) OXYGEN-ION-BOMBARDED SURFACE.

ELECTRON ENERGY

(c) ARGON-SPUTTER-CLEANED SURFACE WITH
REACTED-OXIDE FILM.

Figure 23. - Auger spectra of single-crystal silicon carbide
(0001) surfaces.

(a) Groove and wear debris (surface profile and scanning electron
micrograph).

(b) Wear debris transferred to silicon carbide spherical rider (scan-
ning electron micrograph).

Figure 24. - Wear debris and groove. Single-pass sliding of 0.04-
millimeter-radius silicon carbide rider on pure iron surface;
sliding velocity, 3×10^{-3} m/min; load, 0.25 N; room temperature;
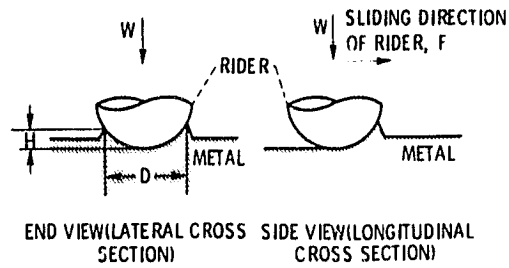environment argon; pressure, atmospheric.
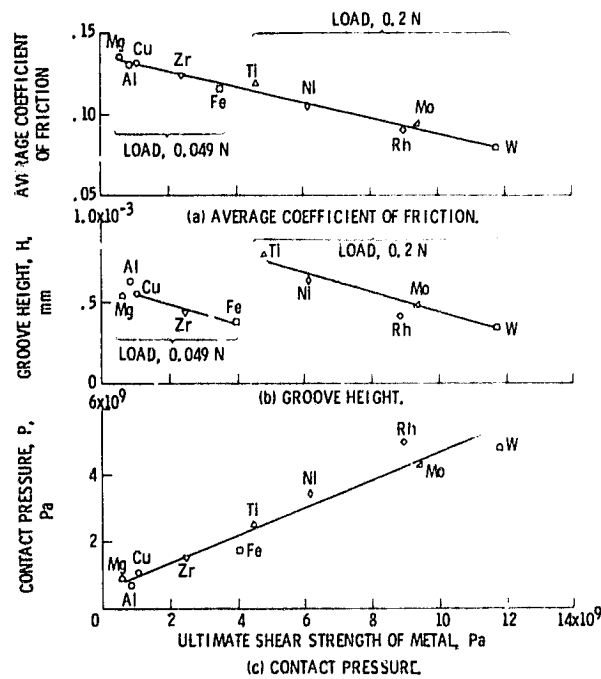
Figure 25. - Deformation of metal.

Figure 26. - Coefficient of friction, groove height, and contact pres-
sure as a function of shear strength for various metals as a result
of single-pass sliding of 0.025-millimeter-radius silicon carbide
rider in mineral oil. Sliding velocity, 3×10^{-3} m/min; load, 0.049
or 0.2 N; room temperature.